# Effect of particle microstructure and the role of proton on the lithium insertion properties of HTiNbO5 electrode material

Etienne Le Calvez, Nicolas Dupré, Éric Gautron, Camille Douard, Olivier Crosnier, Thierry Brousse

# Effect of particle microstructure and the role of proton on the lithium insertion properties of $HTiNbO_5$ electrode material

Etienne Le Calvez[1,2], Nicolas Dupré[1], Éric Gautron[1], Camille Douard[1,2], Olivier Crosnier[1,2*], and Thierry Brousse[1,2]*

[1] Nantes Université, CNRS, Institut des Matériaux Jean Rouxel, IMN, F-44000 Nantes, France

[2] Réseau sur le Stockage Electrochimique de l'Energie (RS2E), CNRS FR 3459, 33 rue Saint Leu, 80039 Amiens Cedex, France

*Correspondence to: thierry.brousse@univ-nantes.fr and Olivier.crosnier@univ-nantes.fr

**Keywords:** Li-ion batteries, high-rate negative electrode, ion exchange, fast intercalation, *in situ* XRD, *ex situ* MAS NMR

**Highlights:**

- Synthesis of three different morphologies of $HTiNbO_5$ has been carried out (Solid state, sol-gel, exfoliation-restacking methods)
- High-resolution electron microscopy demonstrates niobium and titanium ordering in ($MO_6$) octahedral sites.
- The impact of the microstructure on lithium ion intercalation in $HTiNbO_5$ has been studied.
- Solid solution mechanism governs lithium intercalation after an initial and irreversible phase change.
- Protons play a key role on lithium intercalation at high rates.

## Abstract

Layered oxides showing edge-sharing octahedra are promising negative electrode materials for high-power Li-ion batteries. In this sense, we propose the synthesis of the lamellar $HTiNbO_5$ by solid-state (SS), sol-gel (SG) and exfoliation-restacking (NS) syntheses investigating in the same way the charge storage mechanism of this oxide and the influence of the microstructure on material and electrochemical properties. An arsenal of characterization techniques has been used to investigate these three types of particles using X-Ray Diffraction (XRD), electron microscopy, but also by associating mass spectroscopy to thermogravimetric analyses (TGA). Their ability to intercalate lithium has been compared, showing interesting and very similar specific capacities for solid-state and sol-gel synthesis (> 100 $mAh.g^{-1}$ at 0.5 $A.g^{-1}$). In addition, it was shown that the the synthesis giving rise to nanosheet (NS) led to lower performance due to the presence of organic molecules in the interlayer spacing of the 2D lamellar structure. Lastly, *in situ* XRD evidenced a solid-solution reaction for $HTiNbO_5$, with an initial and irreversible phase change leading to the formation of $Li_{0.4}HTiNbO_5$. Moreover, *ex situ* $^1H$ MAS NMR measurements highlight the essential role of the proton in the charge storage mechanism of $HTiNbO_5$. Thus, this paper demonstrates the interest of $HTiNbO_5$ as a fast negative electrode material for high-power Li-ion batteries as well as the predominant role that the proton can play in the diffusion of lithium ions inside a confined interlayer space.

## Introduction

The climate change forces people to use cleaner energies, *i.e.* releasing less greenhouse gases. Thus, renewable energies must be deployed as well as vehicles powered by electric energy thanks to electrochemical storage and conversion devices (batteries and/or fuel cells). In this regard, the batteries need to be charged faster to allow a larger deployment of this technology. It seems necessary to replace the negative graphite electrode in order to charge these electrochemical systems within a few minutes.[1–4] The capacity of graphite is lower during a fast charge (>C) because the insertion of lithium is largely limited by their diffusion in the interlayer space between graphene layers.[5] In addition, graphite inserts lithium ions at a potential that can go below 0.1 V vs $Li^+/Li$. This electrochemical property which allows to achieve high energy density can also lead to the formation of lithium metal in the form of dendrites by lithium plating, resulting in possible short circuits and thermal runaway.[5,6]

Regarding this quest for more powerful devices, different types of materials have been proposed. Among them, niobium and titanium oxides seem to be of interest for such applications.[7–10] The hexagonal form of niobium oxide (T-$Nb_2O_5$) exhibits a capacity of 130 $mAh.g^{-1}$ for a 6 minutes charge while titanium dioxide presents a high theoretic capacity of 335 $mAh.g^{-1}$ for one electron exchanged per transition metal.[10] Even if it is still challenging to achieve high specific capacities, different strategies have been developed to reach the theoretical capacity of $TiO_2$, like the creation of cationic vacancies, fluorine doping, or the reduction of the particle size to improve the ionic and electrical conductivity.[7,8,11,12] Another strategy is to synthesize a metastable form of $TiO_2$, called $TiO_2$(B). After an ionic exchange reaction from $K_2Ti_4O_9$ to $H_2Ti_4O_9$, $TiO_2$(B) is synthesized by a topotactic dehydration reaction of $H_2Ti_4O_9$.[13,14] This material presents edge-sharing octahedra which seems to be an interesting crystallographic feature for fast charging applications.[15] Moreover, it proposes relatively high capacities for fast charging without the need to obtain nanometric particles.[7] In a recent study, Fleichmann *et al.* investigate the electrochemical characteristics of the different intermediate oxides during the dehydration of $H_2Ti_4O_9$ leading to $TiO_2$(B).[16] They demonstrate that partial deprotonation of this oxide offers the highest capacities over a broad range of current densities. Their work sheds light on the impact of protons and water molecules located between the sheets in the charging mechanism of titanium oxides.

During the 1960s and 1970s, Raveau *et al.* studied the ion exchange properties of various niobium, titanium and/or tungsten based multicationic oxides.[17–24] In most cases, the studied materials present interesting intercalation properties. Our previous study proposed the ion exchange of $Rb_2TiNb_6O_{18}$ and the use of the protonated material as an interesting host matrix for lithium intercalation.[25] $H_2TiNb_6O_{18}.2H_2O$ exhibited significantly higher capacities than $Rb_2TiNb_6O_{18}$ as well as a very low (~1%) volume expansion during lithium ion insertion. Among the materials presented by the group of Raveau, $KTiNbO_5$ also offers interesting features. It is a lamellar oxide with 2x2 units of edge-sharing octahedra. These blocks form $(TiNbO_5^-)_n$ layers by corner sharing. Between these layers are located potassium ions. First described by Wadsley[26], $KTiNbO_5$ crystallizes with an orthorhombic lattice in the *Pnma* space group. The material is then described as lamellar along the c direction with cell parameters equal to 6.459 Å, 3.792 Å, 18.742 Å for a, b and c respectively. The titanium ions are mainly located on the internal octahedra of the layers because these are less distorted. Moreover, $KTiNbO_5$ is subject to interesting ion exchange properties. The protons are not surrounded by water molecules. In fact, they are necessary for the stability of the interlayer through the formation of hydrogen bonds with the oxygen atoms in the $(TiNbO_5)$ layers. [22,26]

Thanks to the use of $HTiNbO_5$, we propose to combine the double strategy of using a material based on titanium and niobium having 2x2 units of edge-sharing octahedra but also an oxide offering ionic exchange properties (and so, proton which can help lithium insertion). Several groups have studied this material as a negative electrode for Li-ion batteries. First, in 2008, J-F Colin *et al.* studied lithium intercalation properties of $HTiNbO_5$. They showed the possible insertion of 2 $Li^+$ per formula unit giving rise to $Li_2HTiNbO_5$ between 1.0V and 3.0V *vs* $Li^+/Li$, resulting in a capacity of ~ 240 $mAh.g^{-1}$. A modification of the orientation of the layers is observed in a very similar way to $LiTiNbO_5$.[27] Moreover, the authors proposed a phase change at the beginning of the first lithiation giving rise to $Li_{0.4}HTiNbO_5$, which is irreversibly formed. Lastly, it has been shown that $Li_3HTiNbO_5$ can be formed if this oxide is reduced down to a potential of 0V *vs* $Li^+/Li$ leading to a rocksalt-like structure with very low cyclability. The work of Y. Yuan *et al.* reports on the lithium insertion properties of $HTiNbO_5$ at higher current densities as negative electrode in high-power Li-ion battery.[28] $HTiNbO_5$ is presented as nanowires and exhibits a specific capacity of about 100 $mAh.g^{-1}$ at 5C. An initial phase change is also observed and the following $Li^+$ insertion is

125 governed by a solid solution type mechanism. As this material can be exfoliated, a recent
126 study by J. Zhang *et al.* proposes a study of restacked $HTiNbO_5$ nanosheets in combination
127 with MXenes nanosheets.[29] Specific capacities higher than 100 $mAh.g^{-1}$ at 5 $A.g^{-1}$ have been
128 demonstrated. Nevertheless, no publication reports on the influence of morphologies on the
129 charge storage mechanism and capacities of this oxide. Moreover, no study on the influence
130 of proton in the interlayer on the storage ability of $HTiNbO_5$ has been achieved to date.

131 In the present paper, we study the lithium intercalation behavior of three different
132 microstructures of $HTiNbO_5$ (microparticles, nanoparticles and restacked nanosheets). A
133 systematic investigation of the relationship between the structural, chemical and
134 microstructural properties of the material and their electrochemical characteristics is
135 proposed. Thanks to the use of thermogravimetric analysis (TGA) combined with mass
136 spectroscopy (MS) as well as *in situ* XRD and *ex situ* $^{6}Li$ MAS NMR, we propose a clear
137 understanding of the insertion properties of the different $HTiNbO_5$ samples. Moreover, *ex*
138 *situ* $^{1}H$ MAS NMR provides some clues on the understanding of the influence of protons in
139 the charge storage mechanism of this oxide.

140

141

142

143

144

145

146

147

148

149

150

151

# 1. Experimental section

## a. Synthesis method of $HTiNbO_5$

In this study, $HTiNbO_5$ powder was synthesized in a two-step procedure. First, $KTiNbO_5$ was produced as described below using sol-gel or solid-state route.

### i. Synthesis of $KTiNbO_5$

In the solid-state synthesis method, $Nb_2O_5$ (Alfa Aesar, 99.9%), $TiO_2$ (Alfa Aesar,≥ 99%), and $K_2CO_3$ (ACS Reagent, ≥ 99.0%) precursors were mixed with a molar ratio of 1:2:1.2. Here, a 20% excess of $K_2CO_3$ was added because of its volatility at high temperatures. This mixture was ground in an agate mortar for 10 minutes to obtain a homogeneous powder. This powder was calcined at 1100 °C in a platinum crucible under air for 12 hours to produce $KTiNbO_5$ powder.

In the sol-gel synthesis method, 1.351 mg of $NbCl_5$ (Sigma Aldrich, 99%) was dissolved in 30 mL of ethanol. Separately, 1.703 mg of titanium isopropoxide (Alfa Aesar, 97%) and 0.370 mg of KCl (ACS Reagent, 99.0-100.5%) were dissolved in 200 mL of ethylene glycol. Citric acid (Alfa Aesar, ≥ 99%) was then added to this second solution to achieve a 10:1 molar ratio of citric acid to the total number of cations in the two solutions (Nb, Ti, and K). After stirring for 1 hour to ensure a complete dissolution of all species, the two solutions were mixed, then stirred and heated to 120 °C until forming a blackish gel. This gel was dehydrated at 300 °C in air overnight to ensure complete evaporation of the organic species. It was then calcined at 700 °C in air for 2 hours to produce $KTiNbO_5$ powder.

### ii. Ion exchange $HTiNbO_5$ SS and SG

Ion exchange was performed to obtain $HTiNbO_5$ from $KTiNbO_5$. The final step, common to both SS and SG synthesis, was to mix and stir the $KTiNbO_5$ powder in a 3M $HNO_3$ aqueous solution for 3 days at room temperature. The acidic solution was changed daily to ensure complete exchange of potassium cations by protons. The resulting suspension containing $HTiNbO_5$ powder was then centrifuged and rinsed with DI water until neutral pH of the wastewater was obtained.

### iii. $HTiNbO_5$ nanosheets (NS)

The acid-base reaction of $HTiNbO_5$ SS with tetrabutylammonium ($TBA^+OH^-$) in aqueous solution allows the exfoliation of $(TiNbO_5)^-$ sheets which are then in suspension in this aqueous solution. More precisely, 250mL of aqueous solution at pH=10 containing DI water and TBAOH was prepared. Then, 1g of $HTiNbO_5$ SS powder is introduced for 14 days and stirred. The solution containing suspended $TiNbO_5$ nanosheets is further recovered by centrifugation. The solution contains about $2g.L^{-1}$ of exfoliated particles in suspension. Finally, the nanosheets are restacked by a progressive addition of 0.1M HCl in the solution until complete restacking (pH~4). The obtained $HTiNbO_5$ NS powder was then centrifuged and rinsed with DI water until neutral pH wastewater was obtained. HTiNbO5 SG particles have been exfoliated following similar experimental conditions. HTiNbO5 NS from SG were successfully obtained but the process exhibited an extremely low yield. We attributed this lower reaction yield (in comparison to to HTiNbO5 SS particles) to the smaller size of the particles involving defects on the surface that do not allow a good ionic exchange between the bulky $TBA^+$ cations and the protons. We therefore, do not include electrochemical results concerning such material.

## b. Characterization

### i. Powder X-ray diffraction

X-ray diffraction (XRD) patterns were collected using a PANalytical X'Pert Pro diffractometer (Malvern Panalytical, Almelo, Netherlands). X'Celerator detector with Cu-$K_{\alpha1}$-$K_{\alpha2}$ ($\lambda$ = 1.54060, 1.54439 Å) radiation was used acceleration voltage and current were 40 kV and 40 mA, respectively. With a step scan of 0.0167°, diffraction patterns have been collected between 20° and 80° (2θ). Moreover, i*n situ* XRD patterns have been collected using homemade Leriche-like cell.[30] During charge-discharge experiment, a current of 0.02 $A.g^{-1}$ was applied during 60 min and relaxed during 30 min for XRD pattern acquisition.

### ii. Electron microscopy

Scanning electron microscopy (SEM) images were obtained obtained using a Zeiss MERLIN Instrument operated at 20 kV using in-Lens annular detector. Samples were prepared by dispersing a small fraction of the powder on a piece of conducting carbon tape. EDX spectra were collected at 8.0 mm working distance using an X-Max 50 $mm^2$ OXFORD Instruments detector.

Scanning/Transmission electron microscopy (S/TEM) was also performed in order to characterize the $HTiNbO_5$ powders synthesized by solid-state or sol-gel methods. Powders were dispersed in ethanol and then deposited on a holey carbon film coated copper grid before insertion in a probe-corrected S/TEM Themis Z G3 (Thermo Fisher Scientific). TEM micrographs were collected at 300 kV using a OneView CMOS camera (Gatan). High-angle annular dark-field (HAADF-STEM) images were acquired at 300 kV, with 20 mrad convergence angle and 39-200 mrad collection angles.

### iii. NMR

For MAS NMR analysis, free-standing electrodes with about 5-10 $mg.cm^{-2}$ were polarized for 10h at different states of charge after performing a cyclic voltammogram (CV) at 0.1 $mV.s^{-1}$. After disassembling the Swagelok in a glove box, electrodes were rinsed with a few drops of DMC and then dried overnight under *vacuum* in a Büchi oven at 60°C. Then, the electrolyte-free electrode was placed in a 2.5 mm-diameter zirconia rotor for MAS NMR experiments. $^{7}Li$, $^{6}Li$ and $^{1}H$ MAS NMR spectra were acquired on a Bruker Avance 200 spectrometer ($B_0$ = 4.7 T, Larmor frequencies $\nu_0$ ($^{7}Li$ = 77.78 MHz, $^{6}Li$ = 29.45 MHz and $^{1}H$ = 200.15 MHz) at RT. A Bruker MAS probe with a cylindrical 2.5 mm (o.d) zirconia rotor spun at a frequency of 30 kHz was used. $^{7}Li$ Spectra were obtained by applying a single pulse sequence with a recycle delay (D1) of 3s. $^{6}Li$ Spectra were obtained by applying a synchronized echo sequence with a recycle delay of 3s. $^{1}H$ Spectra were obtained by applying a single pulse sequence with a recycle delay of 30s. D1 values were chosen to ensure the acquisition of quantitative spectra. Integrated intensities were determined by using spectral simulation (DMFit Software).[31] The resulting integrated intensities were normalized with respect to the mass of the sample contained in the NMR rotor, the number of scans, and the receiver gain.

### iv. Electrochemistry

To shape the material, self-supported electrodes were fabricated by mixing, with a small amount of ethanol, 75%wt $HTiNbO_5$, 15%wt of conductive carbon (Carbon Black by Superior Graphite, Chicago, IL, USA) to increase electronic conductivity and 10%wt poly (1,1,2,2-tetrafluoroethylene dissolved in water (PTFE, Sigma Aldrich) to form a homogeneous paste. This mixture was mixed in a mortar to homogenize the solution and then cold-rolled until the obtention of electrodes with a weight of about 5-10 $mg.cm^{-2}$ according to the

requirements enabling the determination of reliable gravimetric values.[32] Using Swagelok cells, electrochemical measurements were performed by separating positive electrode and metallic lithium (99.9%, Aldrich) with a 675 µm thick glass fiber membrane (10 mm diameter, GF/D Whatman) soaked with 1M $LiPF_6$ dissolved in 1:1 %wt. EC/DMC (Solvionic, France, battery grade purity). The cells were assembled in a glove box containing less than 0.1 ppm of $O_2$ and $H_2O$. A VMP3 potentiostat (Biologic operated under ECLab software version V11.36) was used for electrochemical measurements.

## 2. Results and discussion

### a. Materials characterization

In this work, three different $HTiNbO_5$ samples are presented: $HTiNbO_5$ synthesized by solid-state route (called $HTiNbO_5$ SS), restacked $HTiNbO_5$ nanosheet particles obtained by the exfoliation of $HTiNbO_5$ SS particles (designated as $HTiNbO_5$ NS), and a sample called $HTiNbO_5$ SG synthesized by sol-gel process using the Pechini method. This nomenclature will be used throughout the entire paper.

As described in the introduction for its analog $KTiNbO_5$ and in Figure 1, $HTiNbO_5$ is a lamellar oxide with 2x2 units of edge-sharing octahedra. The presence of protons as well as the strong O-H bonds allow this oxide to be considered as an acid.[24] It is the reason why insertion of basic organic molecules by acid-base reaction is possible, such as butylamine as explained in Supplementary Information.[33–35] Moreover, due to the decrease of the interlayer distance after the ion exchange (from c = 18.742 Å for $KTiNbO_5$ to c = 16.656 Å for $HTiNbO_5$), an O-H-O bond is formed between two $(TiNbO_5)_n$ layers.[24] This strengthens the lamellar structure of this material. To confirm these assessments extracted from literature data[22,24], XRD patterns were obtained for this material. As shown in Figure 2.A, the oxides $HTiNbO_5$ SS and $HTiNbO_5$ SG exhibits similar diffraction pattern that are consistent with those proposed in the literature.[22,24] Thus, these materials will be considered as pure phases with a complete ion exchange due to the absence of peaks corresponding to $KTiNbO_5$. Moreover, EDX analyses confirm the presence of negligible amount of potassium in $HTiNbO_5$ SS and SG (< 1%). Since $HTiNbO_5$ NS was obtained from $HTiNbO_5$ SS, this material can also be considered as pure. Nevertheless, $HTiNbO_5$ NS exhibits different pattern than SS and SG, due to the exfoliation-stacking process. Despite the presence of the (002) peak, the absence of (004) and (008) peaks proves the low ordering of $(TiNbO_5)$ layers in this sample. Moreover,

the average interlayer distance for this microstructure can be calculated from the (002) peak. In this respect, we determine a value of the *c* parameter equal to 16.62 Å, ~18.20 Å, and ~22.21 Å for SS, SG, and NS respectively. These *c* parameters have been calculated from the (002) peak using the Bragg law (Figure 2.B.). The value for SS is very close to the literature data [22,24] thus confirming the interlayer distance decrease after ion exchange process. The different value found for $HTiNbO_5$ SG will be further discussed in the following part concerning thermogravimetric analyses coupled with mass spectroscopy. Moreover, for $HTiNbO_5$ NS, the *c* parameter is also very close to the literature data and can be explained by the disorder created during restacking which results in larger interlayer distance.[36–38]

To corroborate the observations made from XRD patterns, SEM and TEM images of $HTiNbO_5$ SS, SG and NS are shown in Figure 3. A clear lamellar microstructure is observed for the micro size particles of $HTiNbO_5$ SS with a preferential growth along the $\vec{c}$ direction (Figure 3.A-B-C). In the case of $HTiNbO_5$ SG, smaller spherical particles of about 50 nm are observed as shown in Figure 3.(D-E-F). The particles are agglomerated as often observed in the case of sol-gel synthesis using the Pechini method.[39–41] Interestingly, for $HTiNbO_5$ NS, the random stacking of $HTiNbO_5$ sheets is observed by SEM. The SEM/TEM images presented in Figure 3.(G-H-I) demonstrate this assumption although they are also depicting some kind of organization of the nanosheets along the $\vec{c}$ direction which explains the (002) peak presence in the corresponding XRD pattern. Moreover, the high intensity of the (002) diffraction peak compared to the other peaks in the case of $HTiNbO_5$ SS is explained by a preferential growth of particles along the c-axis, unlike what is observed for $HTiNbO_5$ SG.

Figure 4 displays a HAADF-STEM image of $HTiNbO_5$ SS acquired along [110] showing its lamellar structure along $\vec{c}$ direction. The intensities in this image are comparable to those of the simulated one (inset) calculated with the structure given by Rebbah *et al.*[24] This provides further evidences that titanium cations occupy preferential sites in the inner position of the layer as previously mentioned in literature thanks to Rietveld refinement and HRTEM images on $Ti_2Nb_2O_9$.[24,42] The lower distortion of the inner octahedra that favors the presence of $Ti^{4+}$ explains the observed cation ordering in $HTiNbO_5$.[42] Moreover, no staking faults is observed in this sample.

For a better understanding of the difference in the (002) peak position between $HTiNbO_5$ SS, SG and NS, TGA combined with MS has been performed. The TGA analyses show a large difference between SS, SG and NS with respect to mass loss as shown in Figure 5.A. For $HTiNbO_5$ SS, a mass loss of about 1% is observed before 300°C. It can be assigned to the loss of water molecules adsorbed at the surface, and possibly a small amount of structural water. Then, between 300°C and 550°C, a transition from $HTiNbO_5$ to $Ti_2Nb_2O_9$ causes an additional 4% mass loss.[43] This mass loss corresponds to one water molecule ($H_2O$) per chemical formula. *A contrario*, $HTiNbO_5$ SG loses 4% of its mass before the transition to $Ti_2Nb_2O_9$ after 300°C. This higher mass loss is attributed to the presence of about one water molecule per protons in the interlayer. This observation, together with the observed difference in crystallinity, explains the difference between the *c* parameters of SS and SG. The case of $HTiNbO_5$ NS is more complex to analyze because of the almost linear decrease of the mass loss during the analysis. At the end of the experiment (550°C), about 11% of the total mass is lost.

Moreover, mass spectroscopy has been combined to TGA at m/z = 18 to investigate in more details water molecule evaporation (Figure 5.B) and at m/z= 40 to know about $CO_2$ evolution (Figure 5.C). Thanks to these experiments, in the case of $HTiNbO_5$ NS, the mass loss is both related to the evaporation of water molecules (chemisorption, physisorption, and transition to $Ti_2Nb_2O_9$) but also to the loss of $CO_2$. This $CO_2$ emission shows the presence of organic molecule and more precisely of TBAOH used for the exfoliation in the interlayer spacing. This observation helps to highlight one reason why the interlayer distance is higher in $HTiNbO_5$. Lastly, as previously mentioned, we notice that the transition to $Ti_2Nb_2O_9$ occurs around 250-300°C which demonstrates the strength of the O-H bond and the important role of protons to insure the stability of the crystallographic structure.

### b. Electrochemistry

To characterize the potential lithium ion insertion in these materials and compare them, charge-discharge experiments at different current densities have been carried out and are displayed in Figure 6. All electrodes were tested between 1.0V and 3.0V *vs* $Li^+/Li$ to ensure the stability of the materials all over the cycling experiments. Various current densities from 0.02 $A.g^{-1}$ to 2.0 $A.g^{-1}$ were used to evaluate the potential use of these different materials in power applications. At low current density (0.02 $A.g^{-1}$), the first cycle

shows a specific capacity of 204, 318 and 250 mAh.g$^{-1}$ for $HTiNbO_5$ SS, SG and NS respectively (Figure 6(A-B-C)). However, low coulombic efficiency in the first cycle is observed specifically for $HTiNbO_5$ SG and NS, which leads to a decrease in capacity (Figure S1). Thus, during the 3rd cycle at 0.02 A.g$^{-1}$, a specific capacity of 225, 204 and 113 mAh.g$^{-1}$ is observed for $HTiNbO_5$ SS, SG and NS respectively. Such differences between $HTiNbO_5$ NS and the others (SS and SG) can be explained by the steric effect due to the presence of TBAOH molecules in the interlayer space of $HTiNbO_5$ NS which considerably reduces the number of available lithium site even if the interlayer spacing is larger than for SS and SG. Moreover, the low coulombic efficiency of the first cycle indicates that a significant amount of lithium cations is not deinserted, thus impeding the further intercalation of lithium during the subsequent cycles.

Concerning the shape of the charge-discharge curve, we observe in the case of $HTiNbO_5$ SS a pronounced plateau at 1.6 V vs $Li^+/Li$. For $HTiNbO_5$ SG, the insertion of lithium cations takes place in a wider potential range (mostly between 1.7V and 1.3V *vs* $Li^+/Li$) with a lower average potential than for $HTiNbO_5$ SS. In contrast to the other two microstructures, $HTiNbO_5$ NS exhibits a charge-discharge plot almost linear between 1.7 V and 1.0 V vs $Li^+/Li$. The charge storage mechanism that governs lithium insertion in $HTiNbO_5$ will be discussed in more details below, at the light of *in situ* XRD analyses and *ex situ* solid-state MAS NMR. When increasing the current density, a similar decrease of the specific capacity is observed for $HTiNbO_5$ SS and SG, which are exhibiting very similar specific capacities at each current. Despite the supposedly good diffusion of lithium ions in between the exfoliated $HTiNbO_5$ sheets, a lower capacity is observed for $HTiNbO_5$ NS based electrode as shown Figure 6.C. To better visualize the differences between each sample, Figure 6.D indicates their specific capacities as a function of the cycle number at different current densities and for the three different microstructures. Except for the first few cycles, comparable specific capacities are determined for SS and SG electrodes. For example, specific capacities of 149 mAh.g$^{-1}$ at 0.10 A.g$^{-1}$ and 82 mAh.g$^{-1}$ at 1.0 A.g$^{-1}$ are reported for $HTiNbO_5$ SS that represented respectively 65% and 35% of its specific capacity at 0.02 A.g$^{-1}$. For the same currents, $HTiNbO_5$ NS shows specific capacity of only 63 and 25 mAh.g$^{-1}$ respectively. From these observations, we can conclude that the architecture of the nanosheets particles ($HTiNbO_5$ NS) is not adequate as a

fast charging/discharging electrode for high power Li-ion batteries. These low capacities can be assigned to the presence of organic molecule in the nanosheets.

To prove this assumption, the intercalation of organic molecule was performed on $HTiNbO_5$ SS as described in Supplementary Information. Figure S3.A demonstrates the effective presence of butylamine in the interlayer space of $HTiNbO_5$ by comparing the XRD of the material before and after mixing with butylamine. Moreover, Figure S3.B demonstrates that even if the electrode achieves a higher capacity at very low current in the case of butylamine-$HTiNbO_5$, a rapid decrease of the capacity is observed due to the steric effect caused by the presence of these very large organic molecules.[44] These results are in line with the observations made on $HTiNbO_5$ NS. Moreover, Figure S3 displays the poor electrochemical behavior of $KTiNbO_5$ SS showing the non-insertion of lithium due to the presence of the large $K^+$ ions in the interlayer spacing confirming the influence of the intercalated species between the ($TiNbO_5$) layers on electrochemical behavior of the corresponding electrode.

### c. *In situ* XRD

To better understand the charge storage mechanism that governs $HTiNbO_5$ according to the different morphologies, we performed *in situ* XRD for $HTiNbO_5$ SS, SG, and NS. These results are presented in Figure 7. It can be noted that for the $HTiNbO_5$ SS, the preferential growth of the grains only enables the detection of (00l) peaks.[43] Thus, it is not possible to trace the volume change in these materials. However, it is still possible to understand the mechanisms that govern lithium intercalation in $HTiNbO_5$ as well as the differences according to the various microstructures. On one hand, for $HTiNbO_5$ SS we observe an initial phase change during the first lithiation. $Li_{0.4}HTiNbO_5$ phase is irreversibly formed and then the material shows a solid solution type lithiation mechanism during the subsequent charging and discharging steps.[28] This is highlighted by the reversible shift of the (002) peak as shown in Figure 7.A. Moreover, the c parameter decreases during the insertion of lithium ions due to coulombic attraction between the positively charged cations in the interlayer and the negatively charged layers $(TiNbO_5)_n$. On the other hand, when lithium ion are extracted during discharge, the c parameter reversibly increases. Interestingly, $HTiNbO_5$ SG

shows a very similar behavior, with a phase change occuring at the beginning of the first lithiation as shown in Figure 7.B. Indeed, the (011) peak initially at 24° disappears leaving place to another peak at 25.5°. The latter shows the formation of $Li_{0.4}HTiNbO_5$ phase (Equation 1). As for $HTiNbO_5$ SS, after this initial step and irreversible formation of $Li_{0.4}HTiNbO_5$, a solid-solution reaction takes place during the following cycles (Equation 2).

$HTiNbO_5 + 0.4Li^+ + 0.4\ e^- \rightarrow Li_{0.4}HTiNbO_5$ *(first cycle)* **Equation 1**

$Li_{0.4}HTiNbO_5 + xLi^+ + xe^- \leftrightarrow Li_xLi_{0.4}HTiNbO_5$ *(further cycles)* **Equation 2**

The (002) peak shift in $HTiNbO_5$ SG electrode is more easily visible thanks to the top view presented in Figure S4.D. Thus, by comparing the variation of the (002) peak between $HTiNbO_5$ SS and $HTiNbO_5$ SG, we notice that the variation of the c parameter is very similar with an initial change followed by a progressive shift. In the case of $HTiNbO_5$ NS, due to the low crystallinity of the material, it is more complex to trace the Li ion insertion mechanism by *in situ* XRD (Figure 7.C). Nevertheless, we notice that smaller peak shifts are observed during lithiation/delithiation. The (002) peak shows an irreversible shift at the end of the first cycle as seen in Figure 7.C and Figure S4.(E-F). This explains the low coulombic efficiency determined for this material. Also, a gradual decrease of the intensity of the peaks seems to demonstrate a decrease of the crystallinity of the structure which could result in a disorganization of the $(TiNbO_5)_n$ layers, which in turn could hinder lithium ion diffusion between the $(TiNbO_5)$ sheets. To summarize, these *in situ* XRD experiments demonstrate, in the case of $HTiNbO_5$ SS and SG, the formation of a phase described as $Li_{0.4}HTiNbO_5$ during the first lithiation. This phase reversibly inserts lithium ions through a solid solution mechanism. In the case of NS, a disorganization of the layers leads to an amorphization and a decrease of the interlayer distance that, in turn, result in a low coulombic efficiency and low specific capacities.

### d. *Ex situ* solid-state MAS NMR

*Ex situ* solid-state MAS NMR was performed on $HTiNbO_5$ SS at several charge and discharge potentials to follow the evolution of lithium and protons local environments upon cycling (Pristine state, 1.5V, 1.0V and 3.0V *vs* $Li^+/Li$). Related CV are shown in Figure 8.A. Indeed, several groups have demonstrated the importance of solid-state MAS NMR. [45–49] This technique allows to better understand the redox mechanisms, to monitor different lithiation sites population and distribution as well as to evidence the changes in the physico-chemical properties of electrodes for batteries and supercapacitors during charging and discharging processes. Here, $^7Li$ and $^6Li$ *ex situ* MAS NMR give some insight on lithium local environments as well as the reversibility of the process. $^1H$ *ex situ* MAS NMR allows a better understanding of the role of the proton as well as how the proton local environment is altered during the insertion of lithium ions during the solid solution mechanism.

As shown in Figure 8.B, for each potential, the $^7Li$ MAS NMR spectrum displays a relatively broad signal close to 0 ppm. These signals are assigned to lithium ions inserted into the material, based on their relative integrated intensities with respect to the state of charge. Compared to 1.5V, the peak at 1.0V is broader, thus suggesting possible differences in lithium mobility within the material or the existence of a slightly different distribution of lithium local environments. The integrated intensity at 1.5V corresponds to 70% of that at 1.0V. Interestingly, the lithiation-delithiation process is not fully reversible with the presence of a peak for the sample recovered after one cycle (3.0V) corresponding to 14% of the lithium present at 1.0V as calculated in Figure S5. This observation is in good agreement with the results obtained by electrochemistry and by *in situ* XRD where we noticed that part of the lithium inserted at the beginning of the first reduction process is consumed to irreversibly form $Li_{0.4}HTiNbO_5$.

In an attempt to obtain more information on the lithiation sites in this material, $^6Li$ solid-state NMR was performed on $HTiNbO_5$ with the same cycled electrodes. Thanks to Figure 8.C, we can notice that at 3.0V (after one cycle) the material shows two distinct resonances. A first one at 1 ppm, very sparsely populated and another one at -0.5 ppm more populated. *A contrario*, at 1.5V and 1.0V, only an intense non-symmetrical resonance can be observed with a maximum close to 1 ppm. This resonance increases clearly during the lithiation process from 1.5 to 1.0 V. This result indicates that the related lithium local environment corresponds to the main lithiation site. In addition, the signals observed at 1.0

and 1.5 V seem to include a shoulder at approx. -0.5 ppm. This information suggests that the major resonance remaining after delithiation at 3.0V is already present during the lithiation process. We then tentatively assign the resonance at -0.5 ppm to the Li site populated upon the irreversible formation of the $Li_{0.4}HTiNbO_5$ phase during the initial lithiation. The peak at 0.5 ppm could also correspond to lithium in the SEI layer. However, we thought this hypothesis less probable as the electrode never goes below a potential of 1V. The potential at which the SEI starts to form is about 0.8V *vs* $Li^+/Li$. Furthermore, $^{19}F$ MAS NMR spectrum appear to indicate that the amount of LiF (a typical SEI component) is only very weakly observed at 1.0V and even less at 3.0V (Figure S6). In addition, at 3.0V, the less populated site (at 1 ppm) could correspond to lithium that did not deintercalate during the oxidation but different from the 0.4 lithium of $Li_{0.4}HTiNbO_5$. Thus, we can conclude that when the first site (-0.5 ppm) is completed, giving rise to the phase change, the lithium ions that are further intercalated go into a different site (1ppm).

Based on these observations, $^1H$ MAS NMR was also performed on the same electrodes to understand changes in proton local environment in the interlayer space as a function of the amount of associated lithium. In 2004, Takagaki *et al.* reported $^1H$ MAS NMR experiments on $HTiNbO_5$ nanosheet.[50] They assigned a resonance at 12 ppm to the proton in the interlayer space. As shown in Figure 8.D, the pristine $HTiNbO_5$ SS also shows a peak at 12 ppm corresponding to an -OH group of the interlayer space, in agreement with previously reported results. An additional small proton resonance, barely visible, is also superimposed on the empty rotor signal at 7 ppm and is attributed to -OH outside the layers (at the surface of the particles). Interestingly, on electrodes reduced to 1.5V and 1.0V, the 12 ppm resonance peak disappears completely while a new signal at 3.4 ppm appears. This indicates that the local environment of all protons present in the interlayer space has changed. The displacement to lower chemical shifts and the narrowing of the resonance indicates more acidic and more mobile protons, respectively. Thus, the lithiation process implies a movement and reorganization of the interlayer protons, due to the insertion of lithium ions. The higher mobility of the protons suggests that the insertion of lithium in the interlayer space leads to a greater instability of the protons in the structure. After one full cycle of the material to 3V, two signals corresponding to protons are observed (Figure 8.D). The resonance at 12 ppm reappears and indicates the presence of protons with a local

environment very similar to the pristine material. This resonance is nevertheless much less intense compared to the case of the pristine material, consistent with a partial reversibility of the redox reaction. Another resonance at 5.6 ppm, wider and more intense than the one at 12 ppm, implies the presence of protons that are more acidic than those in the pristine material but less mobile than the protons in the samples lithiated to 1.5 and 1.0V, suggesting an intermediate state of local environment. Overall, these observations also seem to confirm the irreversible phase change observed by *in situ* XRD. Lastly, $^{1}$H MAS NMR on the pristine $HTiNbO_5$ SG has been performed (Figure S7). It shows very similar properties (acidity and mobility) of protons that the $HTiNbO_5$ SS. This provides an additional argument to explain the observed electrochemical similarities between $HTiNbO_5$ SS and $HTiNbO_5$ SG.

## Conclusion

This work reports on the synthesis and the characterizations of different microstructures of $HTiNbO_5$ with special care to their electrochemical properties. Microparticles (SS), nanoparticles (SG) as well as restacked nanosheets (NS) present different amounts of water in the interlayer space according to XRD and TGA coupled with MS. The similar electrochemical behavior of nano- and microparticles is explained by the very close charge storage mechanism with an initial and irreversible phase change to form $Li_{0.4}HTiNbO_5$, followed by continuous solid-solution reaction during subsequent cycles. $^{1}$H solid state MAS NMR on $HTiNbO_5$ SS highlights the importance of proton in the interlayer spacing for the fast charging abilities of this oxide. In fact, change in the proton properties seems to help the Li ion intercalation by being more mobile and more acidic. In contrast, nanosheet microstructure shows a very poor electrochemical activity because of the organic molecule in its interlayer space. An exfoliation process of $HTiNbO_5$ without the use of organic molecule as exfoliation agent can be of interest to increase the electrochemical performance of $HTiNbO_5$ nanosheet (NS). Nevertheless, several insightful conclusions can be extracted from this work. First, in contrast to $Ti_2Nb_2O_9$, nanosizing the structure does not seem to be useful and effective to achieve higher specific capacity at high rate.[43] This is explained by the main role that protons are playing in the charge storage mechanism. Subsequently, it can be interesting to complete this type of study on other materials made up of protons to generalize the assumptions proposed here. More globally, layered materials presenting

protons in their interlayer spaces can be materials of choice as negative electrode for next generation of high rate Li-ion batteries.

**Acknowledgements**

The authors want to thank Nantes Université and NExT program for financial funding. Marion Allart is also thanked for her assistance for microscopy analysis and Stéphane Grolleau for his help for TGA, MS. As well, ELC, TB and OC thank Guillaume Rogez for his great advices on intercalation of organic molecule in layered inorganic materials as $HTiNbO_5$. The authors would like to acknowledge Nantes Université/NExT program (ANR-16-IDEX-0007, DISCUSS project) and Labex STORE-EX (ANR-10-LABX-76-01) for financial support. Funded by the French Contrat Plan État-Région and the European Regional Development Fund of Pays de la Loire, the CIMEN Electron Microscopy Center in Nantes is greatly acknowledged.

## Figures

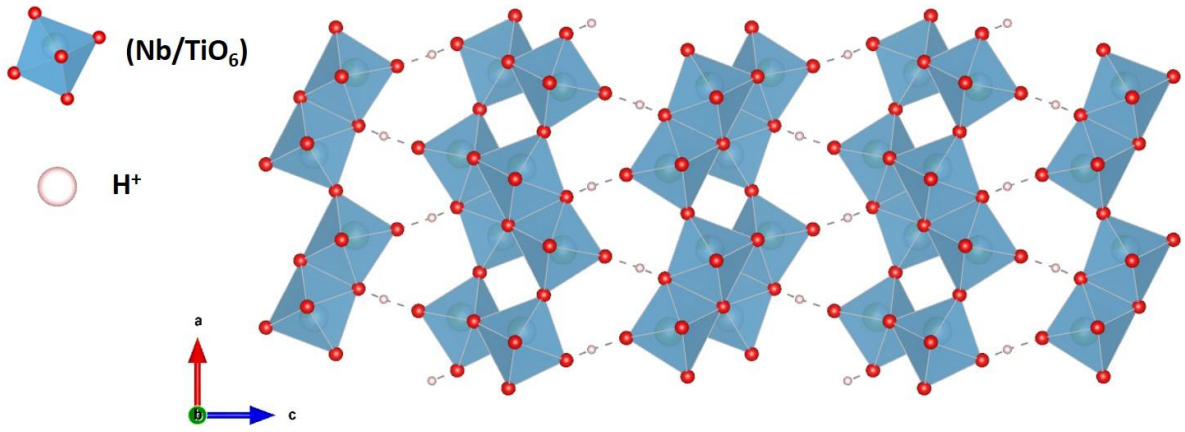


**Figure 1. Crystal structure of $HTiNbO_5$ projected along b axis.[24] $(TiNbO_5)_n$ layers are built up by the formation of 2x2 blocks of edge-sharing octahedra that combine together the edges to form the layers. In between, protons can be found forming hydrogen bonds with oxygen from the layer. It is shown with the use of VESTA.[51]**

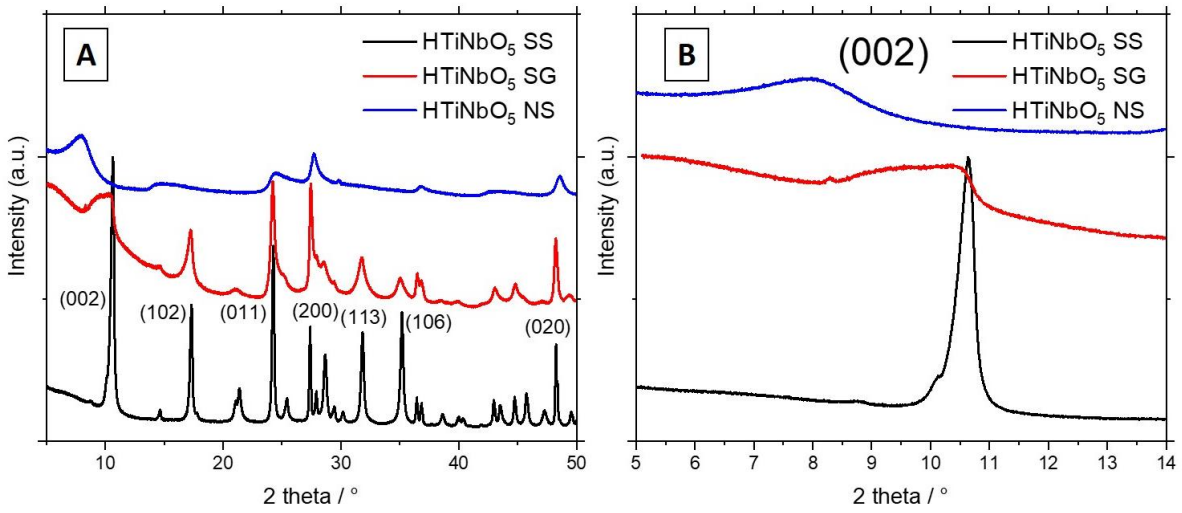


**Figure 2. XRD pattern of $HTiNbO_5$ for the three different morphologies (SS/SG/NS) between (A) 5-50° and (B) 5-14° 2θ angles. XRD patterns highlight the difference in the interlayer distance thanks to the (002) peak shift.**

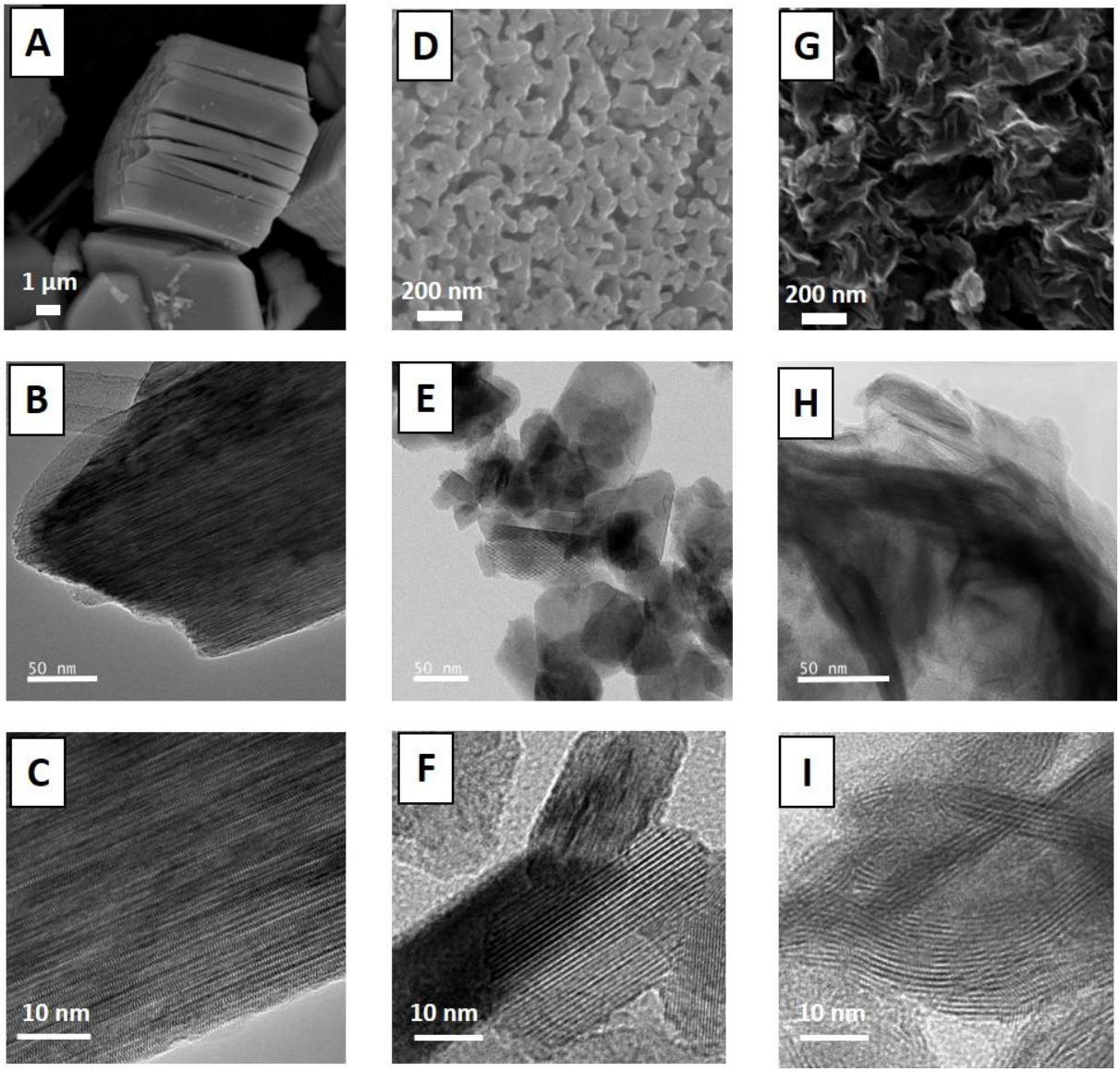


**Figure 3. SEM and TEM images of (A-B-C) $HTiNbO_5$ solid-state (SS) (D-E-F) $HTiNbO_5$ sol-gel (SG) (G-H-I) $HTiNbO_5$ nanosheets (NS).**

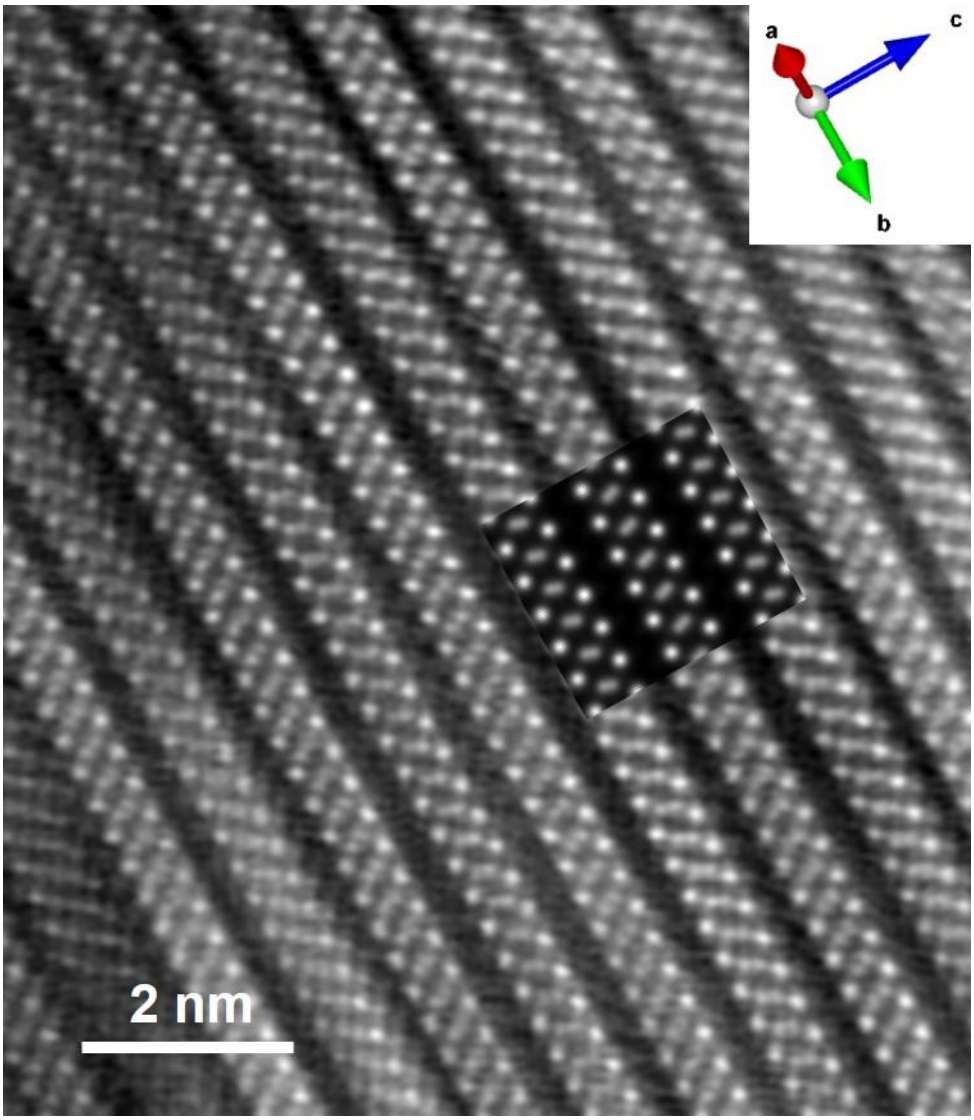


**Figure 4. Experimental HAADF-STEM image (Radial Wiener Filtered) of $HTiNbO_5$ SS viewed along [110] (scale bar: 2 nm). Inset : simulated HAADF image (Dr Probe[52], using ICSD file #31797 [24] as input structure).**

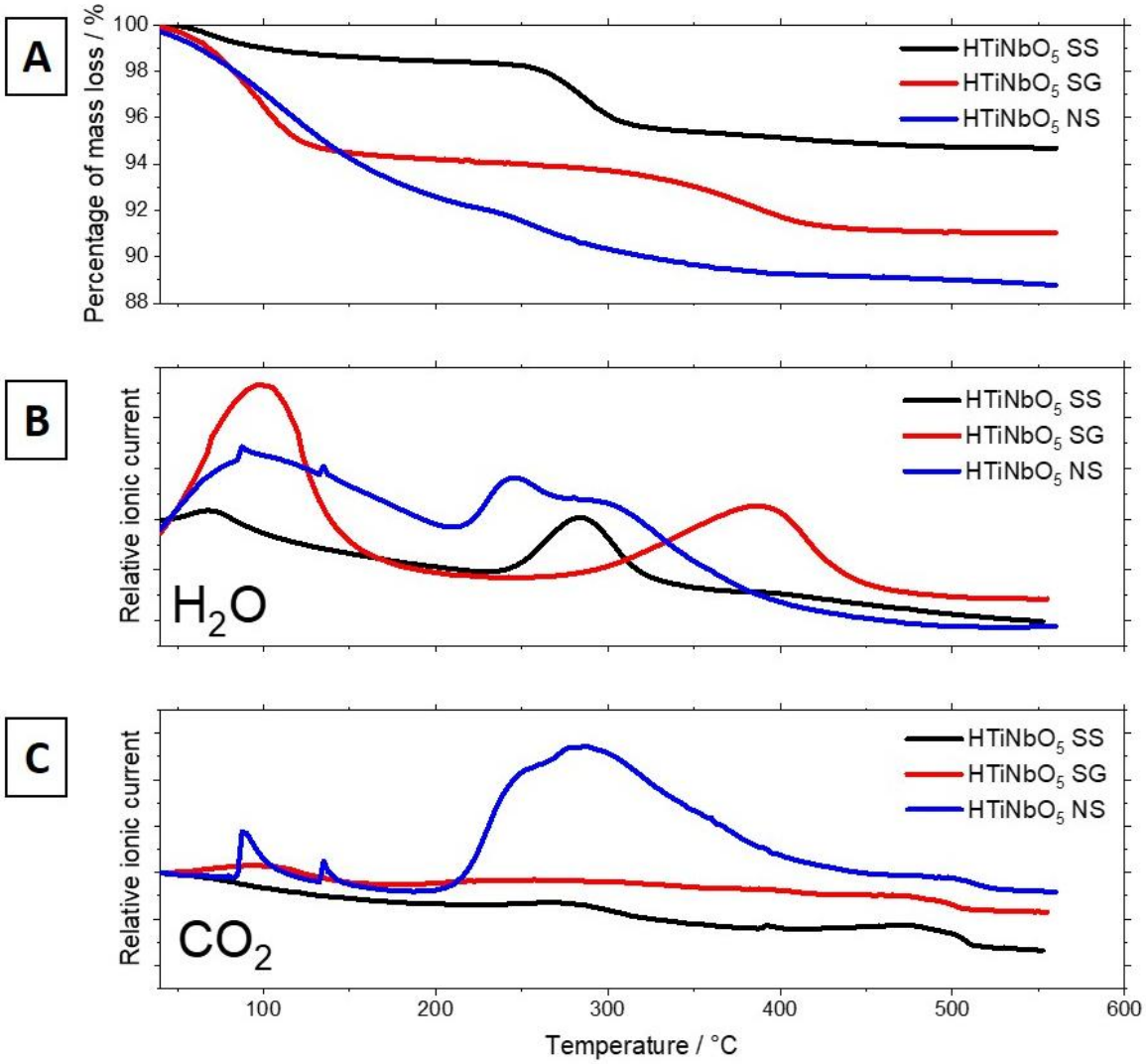


581

582 **Figure 5. (A) Thermogravimetric analysis of the three different morphologies (SS/SG/NS) coupled**
583 **with corresponding mass spectroscopy following different species (B) $H_2O$ (m/z=18) and (C) $CO_2$**
584 **(m/z=40)**

585

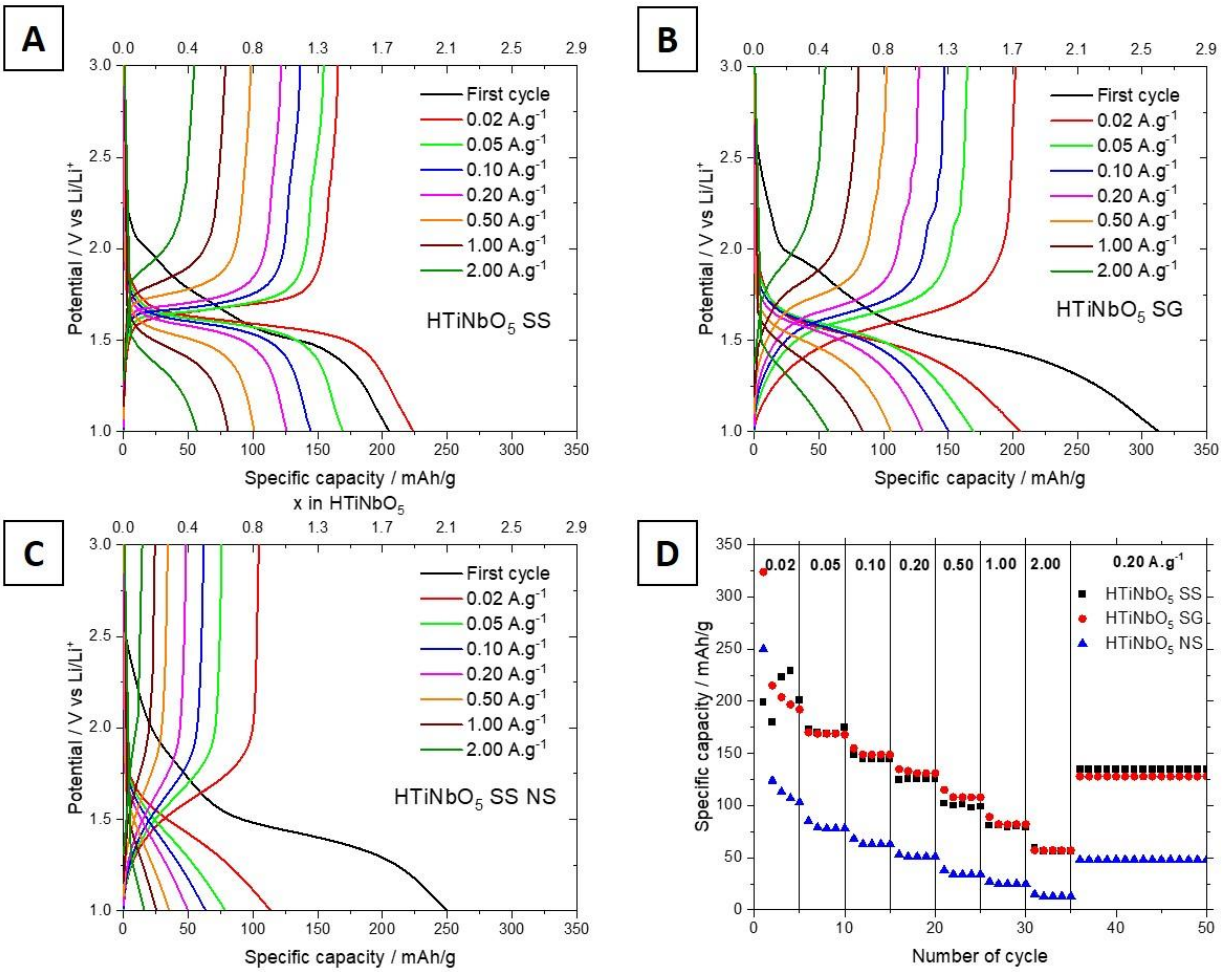


**Figure 6. Charge-discharge experiments at different current densities for (A) $HTiNbO_5$ solid-state (SS) (B) $HTiNbO_5$ sol-gel (SG) (C) $HTiNbO_5$ nanosheet (NS). (D) Capacity *vs* cycle number at different current densities for the three different morphologies (SS/SG/NS) of $HTiNbO_5$**

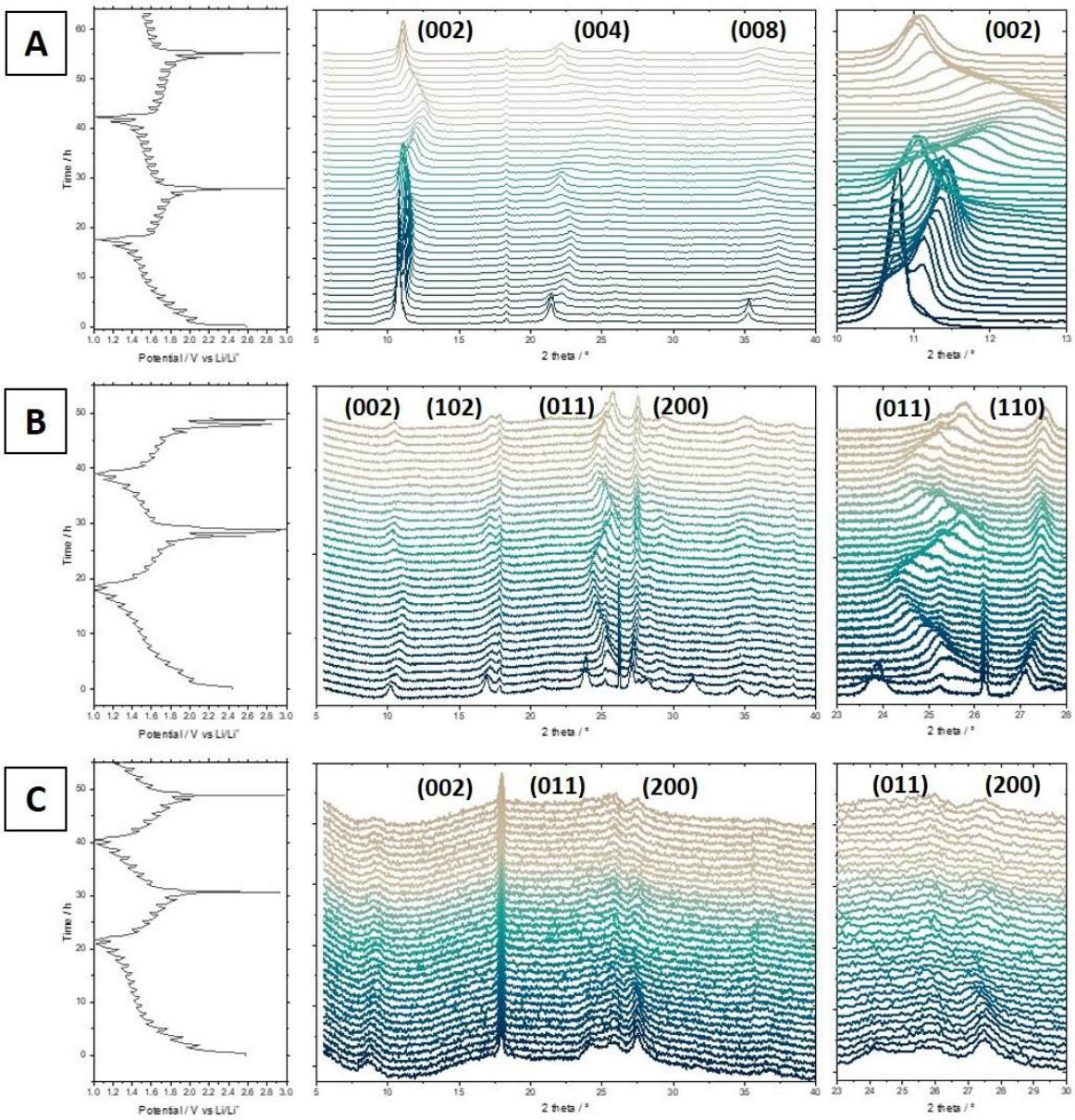


602

603 **Figure 7. *In situ* XRD patterns at a current density of 0.02 A.g$^{-1}$ between 1.0V and 3.0V vs Li$^{+}$/Li of**
604 **(A) $HTiNbO_5$ solid-state (SS) (B) $HTiNbO_5$ sol-gel (SG) (C) $HTiNbO_5$ nanosheets (NS) with**
605 **corresponding voltage-time curves.**

606

607

608

609

610

611

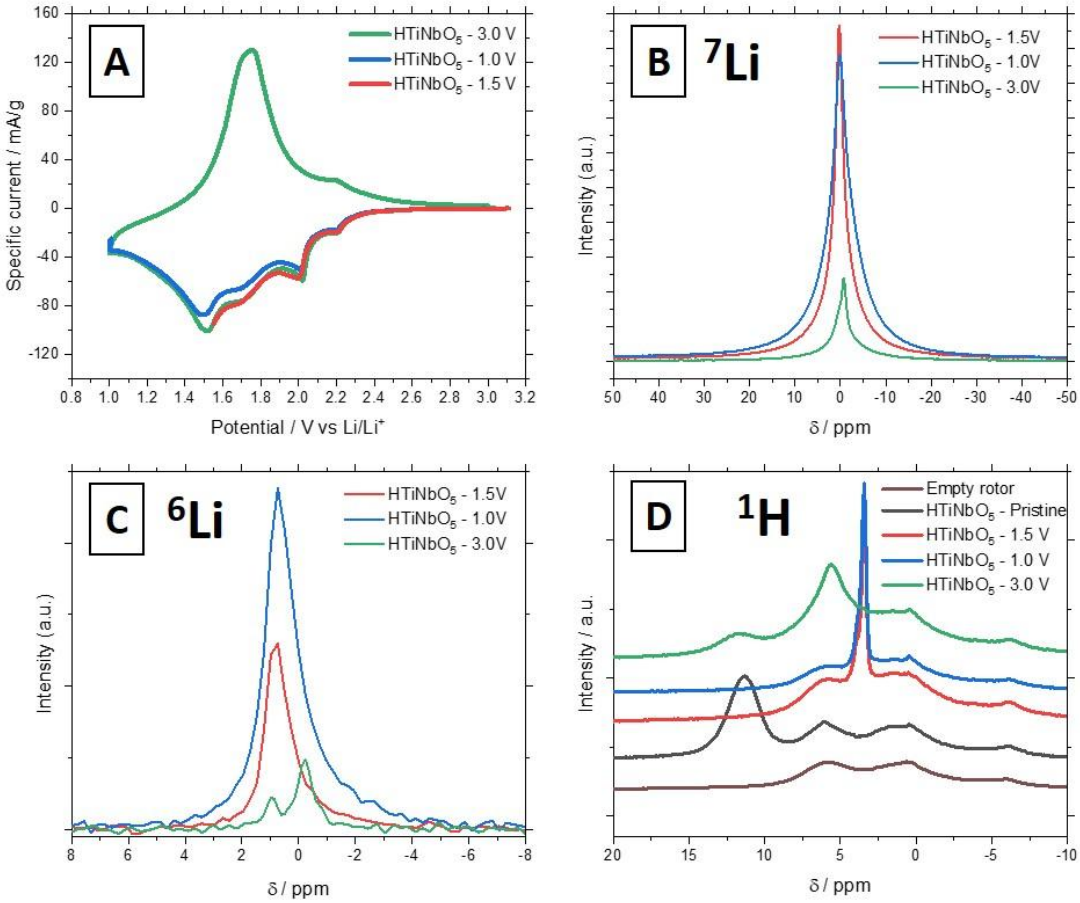


**Figure 8. (A) CV of $HTiNbO_5$ solid-state (SS) at different potential (1.5V/1.0V/3.0V vs $Li^+/Li$). (B) *ex situ* $^7Li$ MAS NMR normalized spectra of $HTiNbO_5$ solid-state (SS) at different potential. (C) *ex situ* $^6Li$ MAS NMR normalized spectra of $HTiNbO_5$ solid-state (SS) at different potential. (D) *ex situ* $^1H$ MAS NMR normalized spectra of $HTiNbO_5$ solid-state (SS) at different potentials.**

## Reference


1. Choi, C. *et al.* Achieving high energy density and high power density with pseudocapacitive materials. *Nat. Rev. Mater.* **5**, 5–19 (2020).
2. Burnham, A. *et al.* Enabling fast charging – Infrastructure and economic considerations. *J. Power Sources* **367**, 237–249 (2017).
3. Li, M., Feng, M., Luo, D. & Chen, Z. Fast Charging Li-Ion Batteries for a New Era of Electric Vehicles. *Cell Rep. Phys. Sci.* **1**, 100212 (2020).
4. Armand, M. & Tarascon, J.-M. Building better batteries. *Nature* **451**, 652–657 (2008).
5. Markovsky, B., Levi, M. D. & Aurbach, D. The basic electroanalytical behavior of practical graphite–lithium intercalation electrodes. *Electrochimica Acta* **43**, 2287–2304 (1998).
6. Aurbach, D. *et al.* Common electroanalytical behavior of Li intercalation processes into graphite and transition metal oxides. *J. Electrochem. Soc.* **145**, 3024 (1998).
7. Beuvier, T. *et al.* $TiO_2$(B) nanoribbons as negative electrode material for lithium ion batteries with high rate performance. *Inorg. Chem.* **49**, 8457–8464 (2010).
8. Wang, J., Polleux, J., Lim, J. & Dunn, B. Pseudocapacitive Contributions to Electrochemical Energy Storage in $TiO_2$(Anatase) Nanoparticles. *J. Phys. Chem. C* **111**, 14925–14931 (2007).
9. Lou, S. *et al.* High-rate capability of three-dimensionally ordered macroporous T-$Nb_2O_5$ through Li+ intercalation pseudocapacitance. *J. Power Sources* **361**, 80–86 (2017).
10. Augustyn, V. *et al.* High-rate electrochemical energy storage through $Li^+$ intercalation pseudocapacitance. *Nat. Mater.* **12**, 518–522 (2013).
11. Moitzheim, S. *et al.* Chlorine doping of amorphous $TiO_2$ for increased capacity and faster Li+-ion storage. *Chem. Mater.* **29**, 10007–10018 (2017).
12. Augustyn, V. *et al.* Lithium-ion storage properties of titanium oxide nanosheets. *Mater. Horiz.* **1**, 219–223 (2014).
13. Marchand, R., Brohan, L. & Tournoux, M. $TiO_2$(B) a new form of titanium dioxide and the potassium octatitanate K2Ti8O17. *Mater. Res. Bull.* **15**, 1129–1133 (1980).
14. Feist, T. P. & Davies, P. K. The soft chemical synthesis of $TiO_2$(B) from layered titanates. *J. Solid State Chem.* **101**, 275–295 (1992).
15. Griffith, K. J., Wiaderek, K. M., Cibin, G., Marbella, L. E. & Grey, C. P. Niobium tungsten oxides for high-rate lithium-ion energy storage. *Nature* **559**, 556–563 (2018).
16. Fleischmann, S. *et al.* Understanding interlayer deprotonation of hydrogen Titanium oxide for high-power electrochemical energy storage. *ACS Appl. Energy Mater.* **2**, 3633–3641 (2019).
17. Gopalakrishnan, J., Bhat, V. & Raveau, B. $AILaNb_2O_7$: A new series of layered perovskites exhibiting ion exchange and intercalation behaviour. *Mater. Res. Bull.* **22**, 413–417 (1987).
18. Jacobson, A. J., Lewandowski, J. T. & Johnson, J. W. Ion exchange of the layered perovskite $KCa_2Nb_3O_{10}$ by protons. *J. Common Met.* **116**, 137–146 (1986).
19. Leclaire, A., Monier, J. C. & Raveau, B. A molybdosilicophosphate with an intersecting-tunnel structure which exhibits ion-exchange properties, $AMo_3P_{5.8}Si_2O_{25}$ (A= Rb, Tl). *Acta Crystallogr. B* **40**, 180–185 (1984).
20. Nedjar, R., Borel, M. M. & Raveau, B. $H_3ONb_3O_8$ and $HNb_3O_8$ : New protonic oxides with a layer structure involving ion exchange properties. *Mater. Res. Bull.* **20**, 1291–1296 (1985).
21. Raveau, B. Ion exchange and intercalation properties for some oxides with a layer and an intersecting tunnel structure. *Rev. Chim. Minérale* **21**, 391–406 (1984).

22. Rebbah, H., Desgardin, G. & Raveau, B. Les oxydes $ATiMO_5$ : Echangeurs cationiques. *Mater. Res. Bull.* **14**, 1125–1131 (1979).
23. Rebbah, H., Hervieu, M. & Raveau, B. The $CsTi_2NbO_7$ type layer oxides: ion exchange properties. *Mater. Res. Bull.* **16**, 149–157 (1981).
24. Rebbah, H., Pannetier, J. & Raveau, B. Localization of hydrogen in the layer oxide $HTiNbO_5$. *J. Solid State Chem.* **41**, 57–62 (1982).
25. Miranda, J., Le Calvez, E., Retoux, R., Crosnier, O. & Brousse, T. Revisiting $Rb_2TiNb_6O_{18}$ as electrode materials for energy storage devices. *Electrochem. Commun.* **137**, 107249 (2022).
26. Wadsley, A. D. Alkali titanoniobates. The crystal structures of $KTiNbO_5$ and $KTi_3NbO_9$. *Acta Crystallogr.* **17**, 623–628 (1964).
27. Colin, J.-F., Pralong, V., Hervieu, M., Caignaert, V. & Raveau, B. New titanoniobates $(Li, H)_2TiNbO_5$ and $(Li, H)_3TiNbO_5$: synthesis, structure and properties. *J. Mater. Chem.* **18**, 3121–3128 (2008).
28. Yuan, Y. *et al.* $H_{0.92}K_{0.08}TiNbO_5$ Nanowires Enabling High-Performance Lithium-Ion Uptake. *ACS Appl. Mater. Interfaces* **11**, 9136–9143 (2019).
29. Zheng, J. *et al.* 2D titanoniobate-titaniumcarbide nanohybrid anodes for ultrafast lithium-ion batteries. *J. Power Sources* **512**, 230523 (2021).
30. Leriche, J. B. *et al.* An Electrochemical Cell for Operando Study of Lithium Batteries Using Synchrotron Radiation. *J. Electrochem. Soc.* **157**, A606 (2010).
31. Massiot, D. *et al.* Modelling one- and two-dimensional solid-state NMR spectra. *Magn. Reson. Chem.* **40**, 70–76 (2002).
32. Gogotsi, Y. & Simon, P. True Performance Metrics in Electrochemical Energy Storage. *Science* **334**, 917 (2011).
33. Kikkawa, S. & Koizumi, M. Organic intercalation on layered compound $KTiNbO_5$. *Mater. Res. Bull.* **15**, 533–539 (1980).
34. Rebbah, H., Borel, M. M. & Raveau, B. Intercalation of alkylammonium ions and oxide layers $TiNbO_5^-$. *Mater. Res. Bull.* **15**, 317–321 (1980).
35. Grandin, A., Borel, M. M. & Raveau, B. Intercalation of primary diamines and amino acid in the layer structure oxide $HTiNbO_5$. *J. Solid State Chem.* **60**, 366–375 (1985).
36. Lin, H.-Y. & Chang, Y.-S. Photocatalytic water splitting on Au/$HTiNbO_5$ nanosheets. *Int. J. Hydrog. Energy* **39**, 3118–3126 (2014).
37. Zhai, Z. *et al.* Thermostable nitrogen-doped $HTiNbO_5$ nanosheets with a high visible-light photocatalytic activity. *Nano Res.* **4**, 635–647 (2011).
38. Takagaki, A. *et al.* Exfoliated nanosheets as a new strong solid acid catalyst. *J. Am. Chem. Soc.* **125**, 5479–5485 (2003).
39. Hench, L. L. & West, J. K. The sol-gel process. *Chem. Rev.* **90**, 33–72 (1990).
40. Huízar-Félix, A. M., Hernández, T., de la Parra, S., Ibarra, J. & Kharisov, B. Sol–gel based Pechini method synthesis and characterization of $Sm_{1-x}Ca_xFeO_3$ perovskite $0.1 \leq x \leq 0.5$. *Powder Technol.* **229**, 290–293 (2012).
41. Li, Y., Yao, S., Wen, W., Xue, L. & Yan, Y. Sol–gel combustion synthesis and visible-light-driven photocatalytic property of perovskite $LaNiO_3$. *J. Alloys Compd.* **491**, 560–564 (2010).
42. Drozhzhin, O. A. *et al.* Revisited $Ti_2Nb_2O_9$ as an Anode Material for Advanced Li-Ion Batteries. *ACS Appl. Mater. Interfaces* **13**, 56366–56374 (2021).
43. Zhou, Y.; Le Calvez, E.; Baek, S. W.; Frajnkovič, M.; Douard, C.; Gautron, E.; Crosnier, O.; Brousse, T.; Pilon, L. Effect of Particle Size on Thermodynamics and Lithium Ion Transport in Electrodes

Made of $Ti_2Nb_2O_9$ Microparticles or Nanoparticles. *Energy Storage Mater.* **2022**, *52*, 371–385. https://doi.org/10.1016/j.ensm.2022.08.010.

44. Thomas, C. I., Heiska, J., Garg, N. & Karppinen, M. Chemical intercalation and electrochemical deintercalation of 2-aminoterephthalic acid into the layered titanoniobate $HTiNbO_5$. *Solid State Ion.* **360**, 115535 (2021).
45. Pecher, O., Carretero-González, J., Griffith, K. J. & Grey, C. P. Materials' methods: NMR in battery research. *Chem. Mater.* **29**, 213–242 (2017).
46. Hope, M. A. *et al.* NMR reveals the surface functionalisation of $Ti_3C_2$ MXene. *Phys. Chem. Chem. Phys.* **18**, 5099–5102 (2016).
47. Grey, C. P. & Dupré, N. NMR studies of cathode materials for lithium-ion rechargeable batteries. *Chem. Rev.* **104**, 4493–4512 (2004).
48. Forse, A. C., Merlet, C., Griffin, J. M. & Grey, C. P. New perspectives on the charging mechanisms of supercapacitors. *J. Am. Chem. Soc.* **138**, 5731–5744 (2016).
49. Forse, A. C. *et al.* Direct observation of ion dynamics in supercapacitor electrodes using in situ diffusion NMR spectroscopy. *Nat. Energy* **2**, 1–7 (2017).
50. Takagaki, A. *et al.* Titanium niobate and titanium tantalate nanosheets as strong solid acid catalysts. *J. Phys. Chem. B* **108**, 11549–11555 (2004).
51. Momma, K. & Izumi, F. VESTA: a three-dimensional visualization system for electronic and structural analysis. *J. Appl. Crystallogr.* **41**, 653–658 (2008).
52. Barthel, J. Dr. Probe: A software for high-resolution STEM image simulation. *Ultramicroscopy* **193**, 1–11 (2018).